GEOPHYSICAL RESEARCH LETTERS, VOL. 36, L17306, doi:10.1029/2009GL039781, 2009

Reactivation of an Archean craton: Constraints from P- and S-wave tomography in North China

Liang Zhao,[1] Richard M. Allen,[2] Tianyu Zheng,[1] and Shu-Huei Hung[3]

Received 25 June 2009; revised 24 July 2009; accepted 28 July 2009; published 4 September 2009.

[1] The unusual reactivation of the North China Craton (NCC) challenges the classical views concerning the strength and stability of cratonic lithosphere. By using teleseismic body-waves recorded at 250 seismic stations, this paper presents high-resolution North China Models of P- and S-wave velocity based on finite-frequency kernel tomography. Both P- and S-wave velocity models reveal that: (1) an obvious N–S trending narrow low-velocity region is located at the base of the lithosphere beneath the Central Block (CB) of the NCC, which extends to more than 500 km depth; (2) a region of high-velocity extends to more than 250–300 km depth beneath the Western Block, in contrast to the much shallower high-velocity zones beneath the CB and shallower high-velocities beneath the Eastern Block. These features suggest that warm mantle material with a source at least as deep as the transition zone, possibly a mantle plume, may be responsible for the reactivation of the NCC. The Central Block may have behaved as a sublithospheric corridor for the warm mantle material due to its pre-existing weakness. **Citation:** Zhao, L., R. M. Allen, T. Zheng, and S.-H. Hung (2009), Reactivation of an Archean craton: Constraints from P- and S-wave tomography in North China, *Geophys. Res. Lett.*, *36*, L17306, doi:10.1029/2009GL039781.

1. Introduction

[2] Continental extension is a major plate tectonics process occurring in a variety of tectonic settings including late to post-orogenic collapse, back-arc spreading or rifting [*Ruppel*, 1995]. Cratonic nuclei, representing stiff rheological heterogeneities within a continental plate, often induce stress concentration and strain localization at their boundaries [*Tommasi and Vauchez*, 2001], but internally remain stable over very long geological periods. However, multiple lines of evidence including geological, geochemical and geophysical observations, have suggested that the thick lithosphere of the Archean North China craton (NCC) was reactivated and rifted during the period from the Late Mesozoic to Cenozoic [*Fan and Menzies*, 1992; *Menzies et al.*, 1993; *Wu et al.*, 2008, and references therein]. The unusual reactivation of the NCC thus challenges the classical views concerning the strength and stability of cratonic lithosphere.

[3] The NCC is traditionally considered the Chinese part of the Sino-Korean craton, which contains some of the oldest known continental rocks, some as old as 3.8 Ga [*Liu et al.*, 1992] (Figure 1). It is proposed that the NCC formed in Paleoproterozoic by the amalgamation of two Archean blocks, the Eastern and Western Blocks (EB and WB), along the Central Block (CB) [e.g., *Zhao et al.*, 2001; *Faure et al.*, 2007]. Previous P-to-S receiver function [*Ai and Zheng*, 2003; *Chen et al.*, 2006; *Chen and Ai*, 2009; *Zhu and Zheng*, 2009] and tomography studies [*Lebedev and Nolet*, 2003; *Huang and Zhao*, 2006; *Li et al.*, 2006; *Zhao et al.*, 2007; *Sun et al.*, 2008; *Tian et al.*, 2009] argue for a cold mantle transition zone beneath the EB and propose that the subducted slab of the Pacific Plate has reached and stagnated atop the 660-km discontinuity. At the same time, beneath the EB, the large amount of volcanism and high heat flow values reaching 65 mW/m^2 [*Hu et al.*, 2000] favor a warm and reactivating upper mantle. In order to explain both observations, both horizontal convection and vertical ascension models have been proposed [*Yuan*, 1996; *Wu et al.*, 2008, and references therein]. The geodynamic mechanism and depth extent of this NCC reactivation remain controversial. While there is a growing consensus that lithospheric rifting has occurred in the EB and extended to the CB [*Xu et al.*, 2004; *Zhao et al.*, 2008], evidence for the vertical and horizontal distribution of lithospheric reactivation still remains unclear.

[4] High-resolution velocity structure plays an important role to understanding the thermal structure and geodynamic processes within and around the craton. Previous tomographic studies are either only P-wave velocity models [*Tian et al.*, 2009; *Xu and Zhao*, 2009], or on a continental scale with sparse sampling coverage in the NCC [e.g., *Lebedev and Nolet*, 2003; *Huang and Zhao*, 2006; *Li et al.*, 2006; *Zhao et al.*, 2007; *Sun et al.*, 2008]. This study is the first to provide high-resolution imaging of both P- and S- wave velocities in an effort to understand the process of reactivation of an Archean craton.

2. Data and Methodology

[5] The data used in this study were mainly from the North China Interior Structure Project (NCISP). The NCISP consists of five temporary linear sub-array operated from December 2000 to May 2008 (Figure 1). Mostly equipped with Güralp CMG-3ESP or 3T sensors (50 Hz to 30 s, 60 s or 120 s) and REFTEK-72A or 130 data loggers. Each array was deployed for 1–1.5 years (Table S1 of the auxiliary material).[4] In addition, four permanent stations BJT, ENH, SSE and XAN (IRIS/IC) were used as a backbone to tie

---

[1] Seismological Laboratory (SKL-LE), Institute of Geology and Geophysics, Chinese Academy of Sciences, Beijing, China.

[2] Department of Earth and Planetary Sciences, University of California, Berkeley, California, USA.

[3] Department of Geosciences, National Taiwan University, Taipei, Taiwan.

0094-8276/09/2009GL039781

[4] Auxiliary materials are available in the HTML. doi:10.1029/2009GL039781.

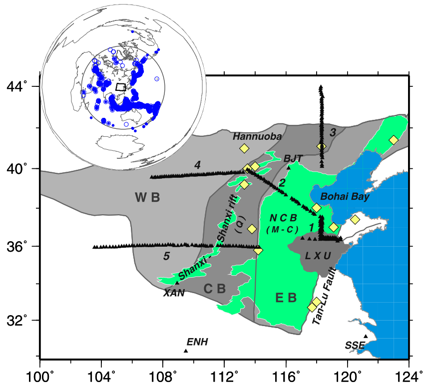

Figure 1. Simplified tectonic map showing major tectonic units of the NCC [after *Zhao et al.*, 2001] and seismic station locations. The triangles mark stations; yellow diamonds represent locations of Cenozoic basalts [*Wu et al.*, 2008, and references therein]; green shadow zone indicate pull-apart basins; numbers indicate the indices of NCISP sub-arrays. EB, Eastern Block; CB, Central Block; WB, Western Block; NCB, North China basin; LXU, Luxi uplift; M-C, Mesozoic-Cenozoic; Q, Quaternary. On the top left inset, locations of events used in this study are marked with open (for P) and solid (for S) blue circles.

together the data from the portable stations that did not overlap temporally [e.g., *Yuan and Dueker*, 2005].

[6] Events with epicentral distance ≥30° were selected. A multi-channel cross-correlation technique [*Vandecar and Crosson*, 1990] was used to measure differential travel times of P and S waves in four frequency bands: 0.02–0.1 Hz, 0.1–0.8 Hz, 0.4–0.8 Hz and 0.8–2.0 Hz. For P phases the 0.4–0.8 Hz band has the best signal-to-noise ratio and contributes 21,853 relative travel-time residuals, which are used in the following imaging. For S waves, 13,619 S phases are selected from 0.02–0.1 Hz band, other bands were dominated by noise. The average standard deviation from cross-correlation is 0.005 sec for P and 0.015 sec for S. The average cross-correlation coefficient is 0.94 for P and 0.93 for S.

[7] The tomographic model space is ~ 2300 km × 2300 km × 2500 km in the east–west, north–south and depth directions respectively, and was centered at (112°E, 37 °N). This space was parameterized with nodes on a ~35 km × 35 km × 39 km grid. The P- and S-wave dataset were used to construct matrices based on both ray theoretical [e.g., *Allen et al.*, 2002] and finite-frequency kernel formulation [*Dahlen et al.*, 2000; *Hung et al.*, 2000]. The LSQR algorithm [*Paige and Saunders*, 1982] was then used to invert the matrix. The damping parameters were determined empirically based on the trade-off between model norm and variance reduction of data. The models discussed in this paper were constructed using damping parameters that yield a variance reduction of ~80% for P wave and ~ 65% for S wave. The advantage of using a simple (1D) background model is that no *a priori* assumptions about the velocity perturbation are made [*Lebedev and Nolet*, 2003]. To account for any baseline shift between the relative travel-time sets for different events, event corrections were included in the inversion as a set of free parameters as were station correction to accommodate velocity anomalies directly beneath each station [e.g., *Allen et al.*, 2002].

3. P- and S-Wave Velocity Models and Resolution Tests

[8] Our results show that structures imaged by finite-frequency kernel methods (Figure 2) and ray-based methods (Figure S1) are very similar except that the kernel-based models yield higher root-mean-square amplitude of P and S wave velocity perturbation as expected [*Hung et al.*, 2004]. Here we focus our discussion on the kernel-based results. The first-order features of our models, for both P- and S-waves, include: (1) A north–south trending narrow low-velocity region with dimension of ~800 km north–south and 200–300 km east–west is located at the base of the CB lithosphere, and extends to more than 300 km depth. The northernmost and southernmost parts extend to more than 500 km depth (e.g., AA′ profile in Figure 2). We note that the north–south continuity of this feature at shallow depths (~100 km) is assumed based on the continuity at greater depths. Continuous resolution at shallow depths is not possible between the two east–west lines. (2) A region of high-velocity extends to more than 250–300 km depth beneath the WB, in contrast to the much shallower high-velocity zones beneath the CB and EB. The P-wave velocity model in this study is broadly consistent with that of *Huang and Zhao* [2006] and *Tian et al.* [2009], except our image exhibits more short-wavelength variations.

[9] The dimensions of the interpreted features in our models are about 200 km or more. To test the ability of the dataset to resolve these structures and the robustness of the solution we conducted multiple resolution tests in which a synthetic 3D velocity model is used to generate synthetic traveltime delays with the same path coverage as the P- and S-wave observed dataset and then inverted to determine if the synthetic velocity structure can be recovered. For each experiment, 10%, 20%, and 30% Gaussian white noise were added in the synthetic relative traveltime residue respectively to represent the noise in the data. The same damping parameters were used in the inversions of the synthetic and observed data. Firstly we conduct checkerboard experiments with alternating high and low velocity anomalies of ±2% δlnVp and ±3% δlnVs with individual block ~210 km × 210 km × 240 km and ~315 km × 315 km × 350 km. The initial synthetic models are shown in Figure S2a–S2h and the recovered models in Figures 3a–3h. The tests show that the resolution is good down to 600 km depth for anomalies ≥200 km even for data with 30% noise in the regions with good sampling coverage. The second test is performed to test how well the dataset can resolve vertical and dipping velocity anomalies. This test uses a dipping low-velocity anomaly with a diameter of 300 km beneath the CB (Figures S2, 3i, and 3k), and a vertical cylindrical low velocity anomaly with a diameter of 160 km beneath the EB (Figures S2, 3j, and 3l). In both anomalies the input velocity perturbations are −2% δlnVp and −3% δlnVs. Inspection of the recovered images shows that the location and shape of the structures are well reconstructed and the downward

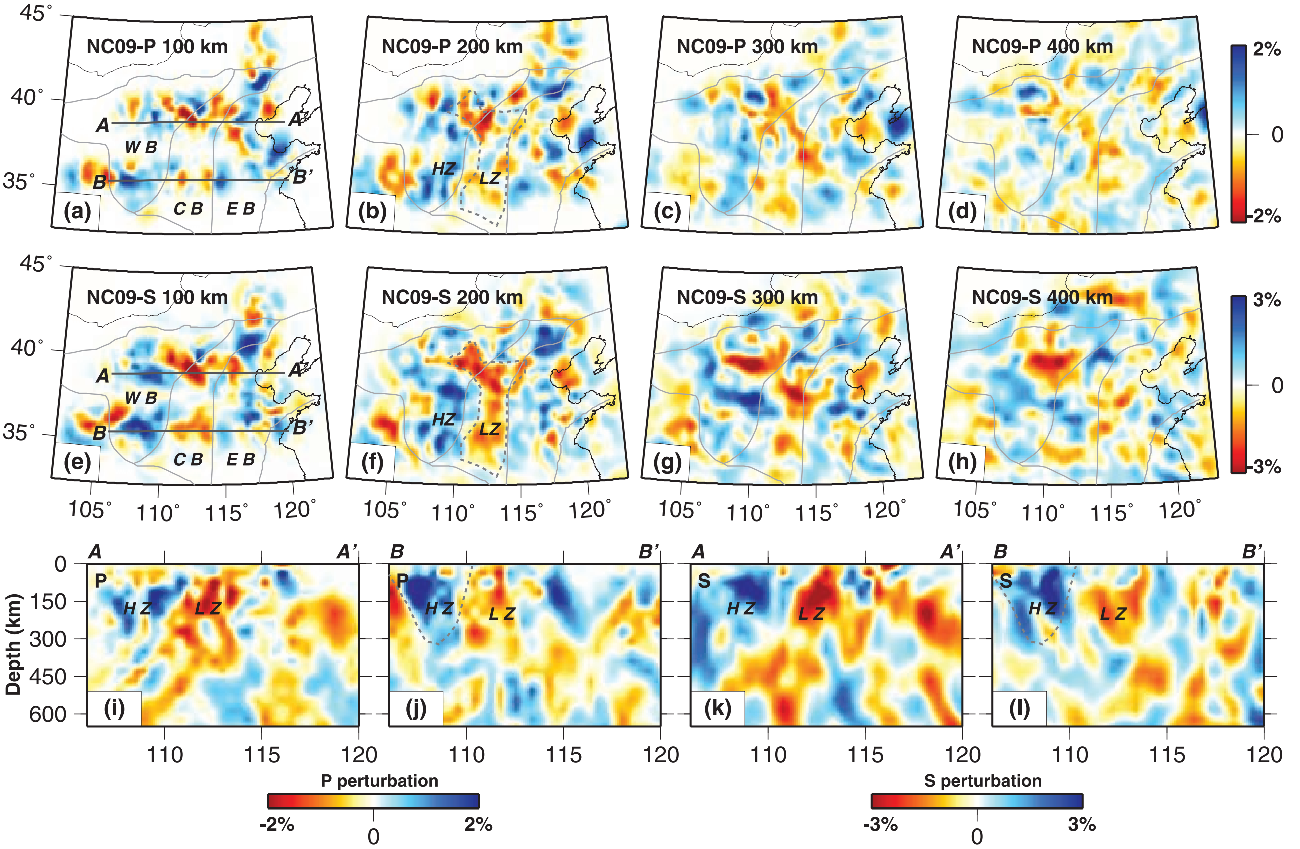

Figure 2. P- and S-wave velocity perturbations resolved from finite-frequency tomography. (a–d) P-wave velocity perturbations at indicated depths. (e–h) S-wave velocity perturbation. Cross sections are presented along A-A′ and B-B′ (i and j) for the P-wave and (k and l) for S-wave model. Closed dash lines on Figures 2b and 2f give the outline of recognized N–S low velocity zone beneath the CB; dash line on Figure 2j represents high-velocity zone beneath the WB. LZ, low-velocity zone; HZ, high-velocity zone.

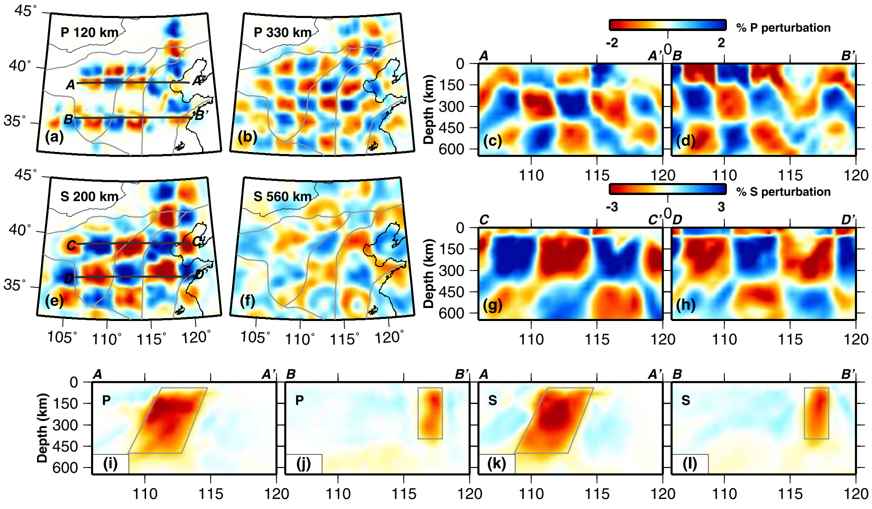

Figure 3. Resolution tests using the available path coverage of differential travel time observations. (a and b) Checkerboard test with ~210 km × 210 km × 240 km blocks for the P-wave dataset. (c and d) Cross sections are presented along A-A′ and B-B′. (e and f) Checkerboard test with blocks of ~315 km × 315 km × 350 km for the S-wave dataset. (g and h) Cross sections are presented along C-C′ and D-D′. (i–l) P- and S-wave vertical resolution tests. Cross sections are along A-A′ and B-B′ marked in Figure 3a. Grey rectangles give the outlines of input cylinder-shape low velocity anomalies. The input synthetic velocity models are shown in Figure S2.

smearing length is less than 50 km. The recovered velocity anomaly amplitudes are slightly reduced.

4. Interpretation and Discussion

[10] Our P- and S-wave velocity images (Figure 2) show evidence for a low velocity anomaly with its parts extending from beneath the base of CB lithosphere to at least 500 km. Most of the known Cenozoic rift systems and basalts (Figure 1) in the region are located above the imaged low velocity zones, including the Shanxi-Shanxi Rift System (SSRS) and the Hannuoba volcanism [e.g., *Tang et al.*, 2006; *Wu et al.*, 2008]. As velocity anomalies within the upper mantle are predominantly caused by temperature anomalies, and >1–1.5% P-wave low velocity anomaly corresponds to a high temperature perturbation exceeding ~100–200 °C [e.g., *Cammarano et al.*, 2003], the imaged low velocities suggest that warm mantle material may be responsible for the reactivation of the Archean NCC. Beneath the CB, the imaged low-velocity anomaly crosses the 410 km discontinuity and extends into the transition zone. This low velocity is aligned with a local ~10 km thinned mantle transition zone relative to a global average imaged by P-to-S receiver functions [*Chen and Ai*, 2009; *Zhu and Zheng*, 2009].

[11] Given that the imaged low-velocity anomaly extends into the transition zone it is unlikely that it is due to small-scale, and therefore shallow, convection processes that might be the result of extensional rifting of the craton. Instead, a deeper source for the low-velocities is required and this deeper source may be responsible for the break-up of the craton. The low-velocity clearly extends into the transition zone based on the presented velocity models, and may or may not continue into the lower mantle. One possible source of the low-velocity is a deep warm mantle plume. Geodynamical models suggest that buoyant upwellings take the form of cylindrical "plumes" rather than sheet-like upwellings. In the upper mantle any upwelling may be modified in geometry by the lithosphere that it impacts, the shape of the cratonic root in this case. Whether the source of the low-velocity is a "plume" or some other process cannot be answered with our study, additional geodynamic, petrological and geochemical efforts may be able to address this in the future.

[12] West of the low velocity anomaly, underlying the WB, a high velocity anomaly extends to >300 km depth. This is likely the cratonic keel of the WB that has apparently remained stable and deflected stress concentration and strain localization to its weaker lithospheric boundaries [e.g., *Tommasi and Vauchez*, 2001].

[13] The geometry of the low-velocity in the upper mantle is modified by the craton geometry inherited from its long geological history of ca 3 Ga. The N–S trend of the low-velocity anomaly between the WB and EB possibly reflects the effect of thick craton lithosphere of the WB on the mantle flow pattern: the ascending mantle flow was deflected after encountering the base of lithosphere and followed a preferred path eroding along the pre-existing weaker lithospheric zone. The CB is a weak zone within the craton as it represents the boundary zone that experienced the stronger ductile deformation and partial melting during the Paleoproterozoic orogeny [e.g., *Zhao et al.*, 2001; *Faure et al.*, 2007; *Trap et al.*, 2009]. Therefore, the CB possibly also behaved as a sublithospheric corridor [e.g., *Duggen et al.*, 2009] for the ascending warm mantle flow resulting in rifting [*Lin and Wang*, 2006] and volcanisms [*Tang et al.*, 2006; *Wu et al.*, 2008] in the Cenozoic. Although tomography image is a snapshot of present earth, we speculate that the weak zones within the cratons possibly had played an important role during the Mesozoic reactivation of the NCC.

[14] The structure of the EB is less clear. The P-velocity model shows a thick high-velocity root, while the S-velocity model shows less of a cratonic root signal (Figure 2). At the eastern margin of the NCC, beneath the Tanlu fault zones in the Luxi uplift (LXU) and the Bohai Bay (see Figure 1), the high-velocity lithosphere is thinner than beneath the craton. P-to-S receiver function studies suggest that the depth of lithosphere-asthenosphere boundary is less than 100 km [*Chen et al.*, 2006; *Zheng et al.*, 2008].

5. Conclusions

[15] Finite-frequency kernel based P- and S-wave velocity images show that a N–S trending low velocity anomaly extends from beneath the CB to at least 500 km. High-velocity anomalies extend to more than 250–300 km depth beneath the WB, and to shallower depths beneath the CB and the EB. The imaged structure suggests that the presence of warm material with a source at least as deep as the transition zone is responsible for reactivation of the NCC. The pre-existing weak zone within the CB of the craton likely acted as a sublithospheric corridor for the warm mantle material.

[16] **Acknowledgments.** This work was completed during L. Zhao's visit to Berkeley Seismological Laboratory sponsored by K.C. Wong Education Foundation, Hongkong. We thank M. Xue, M. Obrebski, H.Y. Yuan, R. Porritt, W.W. Xu and L. Chen for constructive help. We thank E. Calais, M. Faure and an anonymous reviewer for very helpful reviews. Data used were provided by Seismological Laboratory, IGGCAS and IRIS DMC. This research was financially supported by the NSFC grant 90814002. The BSL contribution number is 09-15.

References

Ai, Y., and T. Zheng (2003), The upper mantle discontinuity structure beneath eastern China, *Geophys. Res. Lett.*, *30*(21), 2089, doi:10.1029/2003GL017678.

Allen, R. M., et al. (2002), Imaging the mantle beneath Iceland using integrated seismological techniques, *J. Geophys. Res.*, *107*(B12), 2325, doi:10.1029/2001JB000595.

Cammarano, F., S. Goes, P. Vacher, and D. Giardini (2003), Inferring upper-mantle temperatures from seismic velocity, *Phys. Earth Planet. Inter.*, *138*, 197–222, doi:10.1016/S0031-9201(03)00156-0.

Chen, L., and Y. Ai (2009), Discontinuity structure of the mantle transition zone beneath the North China Craton from receiver function migration, *J. Geophys. Res.*, *114*, B06307, doi:10.1029/2008JB006221.

Chen, L., T. Zheng, and W. Xu (2006), A thinned lithospheric image of the Tanlu Fault Zone, eastern China: Constructed from wave equation based receiver function migration, *J. Geophys. Res.*, *111*, B09312, doi:10.1029/2005JB003974.

Dahlen, F. A., S. H. Hung, and G. Nolet (2000), Fréchet kernels for finite-frequency traveltimes—I. Theory, *Geophys. J. Int.*, *141*, 157–174, doi:10.1046/j.1365-246X.2000.00070.x.

Duggen, S., K. A. Hoernle, F. Hauff, A. Klügel, M. Bouabdellah, and M. F. Thirlwall (2009), Flow of Canary mantle plume material through a subcontinental lithospheric corridor beneath Africa to the Mediterranean, *Geology*, *37*, 283–286, doi:10.1130/G25426A.1.

Fan, W., and M. A. Menzies (1992), Destruction of aged lower lithosphere and accretion of asthenosphere mantle beneath eastern China, *Geotecton. Metal.*, *16*, 171–180.

Faure, M., P. Trap, W. Lin, P. Monié, and O. Bruguier (2007), Polyorogenic evolution of the Paleoproterozoic Trans-North China Belt, new insights from the Lüliangshan-Hengshan-Wutaishan and Fuping massifs, *Episodes*, *30*, 1–12.

Hu, S., L. He, and J. Wang (2000), Heat flow in the continental area of China: A new data set, *Earth Planet. Sci. Lett.*, *179*, 407–419, doi:10.1016/S0012-821X(00)00126-6.

Huang, J., and D. Zhao (2006), High-resolution mantle tomography of China and surrounding regions, *J. Geophys. Res.*, *111*, B09305, doi:10.1029/2005JB004066.

Hung, S., F. A. Dahlen, and G. Nolet (2000), Fréchet kernels for finite-frequency traveltimes—II. Examples, *Geophys. J. Int.*, *141*, 175–203, doi:10.1046/j.1365-246X.2000.00072.x.

Hung, S., Y. Shen, and L. Chiao (2004), Imaging seismic velocity structure beneath the Iceland hot spot: A finite frequency approach, *J. Geophys. Res.*, *109*, B08305, doi:10.1029/2003JB002889.

Lebedev, S., and G. Nolet (2003), Upper mantle beneath Southeast Asia from S velocity tomography, *J. Geophys. Res.*, *108*(B1), 2048, doi:10.1029/2000JB000073.

Li, C., R. Van der Hilst, and M. N. Toksöz (2006), Constraining P-wave velocity beneath Southeast Asia, *Phys. Earth Planet. Inter.*, *154*, 180–195, doi:10.1016/j.pepi.2005.09.008.

Lin, W., and Q. Wang (2006), Late Mesozoic extensional tectonics in the North China block: A crustal response to subcontinental mantle removal?, *Bull. Soc. Geol. Fr.*, *177*, 287–297, doi:10.2113/gssgfbull.177.6.287.

Liu, D., A. P. Nutman, W. Compston, J. Wu, and Q. Shen (1992), Remnants of $\geq$3800 Ma crust in the Chinese part of the Sino-Korean Craton, *Geology*, *20*, 339–342, doi:10.1130/0091-7613[1992]020<0339:ROMCIT>2.3.CO;2.

Menzies, M. A., W. M. Fan, and M. Zhang (1993), Palaeozoic and Cenozoic lithoprobes and the loss of N120 km of Archaean lithosphere, Sino-Korean Craton, China, in *Magmatic Processes and Plate Tectonics*, edited by H. M. Prichard et al., *Geol. Soc. Spec. Publ.*, *76*, 71–78.

Paige, C. C., and M. A. Saunders (1982), LSQR: An algorithm for sparse linear-equations and sparse least-squares, *Trans. Math. Software*, *8*, 43–71, doi:10.1145/355984.355989.

Ruppel, C. (1995), Extensional processes in continental lithosphere, *J. Geophys. Res.*, *100*, 24,187–24,215, doi:10.1029/95JB02955.

Sun, Y., M. N. Toksöz, S. Pei, D. Zhao, F. Dale Morgan, and A. Rosca (2008), S wave tomography of the crust and uppermost mantle in China, *J. Geophys. Res.*, *113*, B11307, doi:10.1029/2008JB005836.

Tang, Y., H. Zhang, and J. Ying (2006), Asthenosphere–lithospheric mantle interaction in an extensional regime: implication from the geochemistry of Cenozoic basalts from Taihang Mountains, North China Craton, *Chem. Geol.*, *233*, 309–327, doi:10.1016/j.chemgeo.2006.03.013.

Tian, Y., D. Zhao, R. Sun, and J. Teng (2009), Seismic imaging of the crust and upper mantle beneath the North China Craton, *Phys. Earth Planet. Inter.*, *172*, 169–182, doi:10.1016/j.pepi.2008.09.002.

Tommasi, A., and A. Vauchez (2001), Continental rifting parallel to ancient collisional belts: An effect of the mechanical anisotropy of the lithospheric mantle, *Earth Planet. Sci. Lett.*, *185*, 199–210, doi:10.1016/S0012-821X(00)00350-2.

Trap, P., M. Faure, W. Lin, and P. Monié (2009), The Zhanhuang Massif the second and eastern suture zone of the Paleoproterozoic Trans-North China Orogen, *Precambrian Res.*, *172*, 80–98, doi:10.1016/j.precamres.2009.03.011.

Vandecar, J. C., and R. S. Crosson (1990), Determination of teleseismic relative phase arrival Times using multi-channel cross-correlation and least-squares, *Bull. Seismol. Soc. Am.*, *80*, 150–169.

Wu, F., Y. Xu, S. Gao, and J. Zheng (2008), Lithospheric thinning and destruction of the North China Craton, *Acta Petrol. Sin.*, *24*, 1145–1174.

Xu, P., and D. Zhao (2009), Upper-mantle velocity structure beneath the North China Craton: Implications for lithospheric thinning, *Geophys. J. Int.*, *177*, 1279–1283, doi:10.1111/j.1365-246X.2009.04120.x.

Xu, Y., S. Chung, J. Ma, and L. Shi (2004), Contrasting Cenozoic lithospheric evolution and architecture in the eastern and western Sino-Korean craton: Constraints from geochemistry of basalts and mantle xenoliths, *J. Geol.*, *112*, 593–605, doi:10.1086/422668.

Yuan, X. (1996), Velocity structure of the Qinling lithosphere and the mushroom cloud model, *Sci. China Ser. D*, *39*, 235–244.

Yuan, H., and K. Dueker (2005), Teleseismic P-wave tomogram of the Yellowstone plume, *Geophys. Res. Lett.*, *32*, L07304, doi:10.1029/2004GL022056.

Zhao, G., S. A. Wilde, P. A. Cawood, and M. Sun (2001), Archean blocks and their boundaries in the North China Craton: Lithological, geochemical, structural and P-T path constraints and tectonic evolution, *Precambrian Res.*, *107*, 45–73, doi:10.1016/S0301-9268(00)00154-6.

Zhao, D., S. Maruyama, and S. Omori (2007), Mantle dynamics of Western Pacific and East Asia: Insight from seismic tomography and mineral physics, *Gondwana Res.*, *11*, 120–131, doi:10.1016/j.gr.2006.06.006.

Zhao, L., T. Zheng, and G. Lü (2008), Insight into craton evolution: Constraints from shear wave splitting in the North China Craton, *Phys. Earth Planet. Inter.*, *168*, 153–162, doi:10.1016/j.pepi.2008.06.003.

Zheng, T., L. Zhao, W. Xu, and R. Zhu (2008), Insight into modification of North China Craton from seismological study in the Shandong Province, *Geophys. Res. Lett.*, *35*, L22305, doi:10.1029/2008GL035661.

Zhu, R., and T. Zheng (2009), Destruction geodynamics of the North China craton and its Paleoproterozoic plate tectonics, *Chin. Sci. Bull.*, *54*, 1–13, doi:10.1007/s11434-009-0451-5.

R. M. Allen, Department of Earth and Planetary Sciences, University of California, Berkeley, 215 McCone Hall, Berkeley, CA 94720, USA. (rallen@berkeley.edu)

S.-H. Hung, Department of Geosciences, National Taiwan University, P.O. Box 13-318, Taipei 106, Taiwan. (shung@ntu.edu.tw)

L. Zhao and T. Zheng, Seismological Laboratory (SKL-LE), Institute of Geology and Geophysics, Chinese Academy of Sciences, Beituchengxi Road 19, P.O. Box 9825, Beijing 100029, China. (zhaoliang@mail.igcas.ac.cn; tyzheng@mail.igcas.ac.cn)